The effects of filling patterns on the powder–binder separation in powder injection molding

CrossMark

Fang Wei, He Xinbo *, Zhang Ruijie, Yang Shidi, Qu Xuanhui

Advanced Materials and Technologies Institute, University of Science and Technology Beijing, Beijing 100083, China

ARTICLE INFO

ABSTRACT

The powder–binder separation is a common difficulty during injection molding, which leads to the inhomogeneity in the debinding and sintering stages. Previous studies focus on the relationship between "final results" and "initial conditions", while the dynamic filling process of feedstock and the evolution of powder–binder separation were ignored. This work investigated the effects of filling patterns on the powder–binder separation during powder injection molding. The mold filling model of PIM has been developed, based on the multiphase fluid theory and the viscosity model of feedstock. Parameters of the viscosity model were modified by the experimental data. Numerical simulations were compared with experiments with the same process parameters. The powder–binder separation phenomena in green bodies were detected by X-Ray computed tomography (CT). The experimental phenomena were explained clearly by the evolution of powder–binder separation obtained with numerical simulation method. A typical compacting filling pattern of PIM and filling mobility variable of the feedstock were proposed. A proper filling pattern was helpful to ensure the mobility of feedstock and the homogeneity of green body.

© 2014 The Authors. Published by Elsevier B.V. Open access under CC BY-NC-ND license.

1. Introduction

Powder injection molding (PIM) is a net-shape-forming technology that provides advantages when making complex-shape parts with high-performance of engineering materials. Typically, there are four stages involved in PIM process, namely mixing, injection molding, debinding and sintering, among which molding is a critical stage for forming a desired shape. The study of the rheological behavior of feedstock is very important to understand the molding process. The feedstock exhibits pseudoplastic or shear thinning flow behaviors, and the properties of feedstock are generally closer to a polymer [1]. A systematic analysis for the effect of binder and powder system on rheological properties was done by Ahn [2], and the results showed that the power law index of viscosity model was more sensitive in binder selection than powder selection. The effects of other factors on rheological properties of feedstock during molding process, such as molding dimensions [3], particle size distribution [4], powder loading [5,6] and process parameters [7,8] were widely reported in the technical literature.

The separation of powder and binder is a common difficulty during injection molding, which may lead to the inhomogeneity in the debinding and sintering stages. The phase separation phenomena could be detected by X-Ray CT [9,10]. Increasing powder content was available to alleviate separation effects [11]. The effect of mold on powder accumulation regions and binder rich regions was discussed by Karatas [12]. Shivashankar [13] proposed a predictor of powder–binder separation, which is based on particle size, particle volume fraction and maximum particle content. The powder–binder separation has been widely investigated, but these studies mentioned in the literature [9,13] were focused on the relationship between "final results" and "initial conditions", sometimes, conflicting conclusions were obtained [11,13]. The dynamic filling process of feedstock and the evolution of powder–binder separation were ignored.

The evolution of powder–binder separation during injection molding is difficult to be detected with experimental method, especially, in the early stage of molding. Numerical calculation method has the advantage in the understanding of material feature evolution during preparation process. Multiphase fluid model has been developed to study the injection molding stage with numerical simulations [14,17]. The modified viscosity model of feedstock based on the experimental data had good effect on the simulations [18,19]. Simulations of powder–binder separation have been done by Kim [15] and Samanta [17], but there was a lack of evolution of powder–binder separation and corresponding systematic analysis.

The purpose of this study was to investigate the influence of filling patterns on the powder–binder separation in powder injection molding. The mold filling model of PIM has been developed, coupling the multiphase fluid theory with viscosity model of feedstock. The viscosity

* Corresponding author.
  E-mail address: xb_he@163.com (X. He).

model of feedstock was modified by the measured experimental data. In order to compare the obtained experimental data with numerical simulation results, the same process parameters were used. The powder–binder separation in the green body was detected by X-Ray CT. The experimental phenomena were explained clearly by the evolution of powder–binder separation obtained by numerical simulation. A compacting filling pattern of PIM and filling variable of feedstock were proposed, and the corresponding quantitative analysis was performed.

2. Model of mold filling

2.1. Powder–binder two-phase model

In PIM, a high powder loading is required, and particles almost touch with each other. Therefore, in this study the powders were hypothesized to be a pseudo-liquid phase that had properties very similar to that of real solid particles. The binder was treated as another liquid phase. The powder pseudo-liquid phase and binder liquid phase follow the continuity equations for mass, momentum and energy.

The mass conservation equation is:

$$\frac{\partial}{\partial t}(\phi_k \rho_k) + \nabla \cdot (\phi_k \rho_k \mathbf{v_k}) = 0. \tag{1}$$

The momentum conservation equation is:

$$\frac{\partial}{\partial t}(\phi_k \rho_k \mathbf{v}_k) + \nabla \cdot (\phi_k \rho_k \mathbf{v_k} \mathbf{v_k}) = -\phi_k \nabla p_k + \nabla \cdot (\phi_k \boldsymbol{\tau}_k) + \phi_k \rho_k \mathbf{g} + \mathbf{F}_k. \tag{2}$$

The energy conservation equation is:

$$\frac{\partial}{\partial t}\left[\phi_k \rho_k \left(e_k + \frac{1}{2}\mathbf{v_k^2}\right)\right] + \nabla \cdot \left[\phi_k \rho_k \mathbf{v_k}\left(e_k + \frac{1}{2}\mathbf{v_k^2}\right)\right] = -\nabla \cdot (\phi_k p_k \mathbf{v_k}) + \nabla \cdot (\phi_k \boldsymbol{\tau}_k \cdot \mathbf{v_k}) - \nabla \cdot (\phi_k q_k) + \phi_k \rho_k \mathbf{g} \cdot \mathbf{v_k} + E_k \tag{3}$$

where k represents either the powder phase or the binder phase and ϕ_k, ρ_k, $\mathbf{v_k}$ and $\mathbf{q}_k$ are the volume fraction, density, velocity and heat flow flux of phase k, respectively.

$\mathbf{F}_k$ is the drag force that results from momentum exchange between both phases. E_k is the source term in the energy equation that takes care energy exchange between the phases.

2.2. Viscosity model of feedstock

Using the appropriate model is helpful to get reliable results of numerical simulation. Koszkul [20] discussed several viscosity models, and the difference mainly concentrated upon viscosities at the very low shear rate range. In this study, the power law model was used to describe the viscosity of feedstock.

$$\eta_f = \eta_b K_{\phi D} \dot{\gamma}^{n-1} \tag{4}$$

where η_f and η_b are the viscosities of feedstock and binder system; $\dot{\gamma}$ is the shear rate and n is the power law index, for polymer melts, $0 < n < 1$. $K_{\phi D}$ is a factor based on the powder loading, particle size and shape. In this study, the powder loading and particle are fixed, and $K_{\phi D}$ is a constant decided by the viscosity experimental data.

The viscosity of each component of the binder is:

$$\eta_{bx} = \eta_{0x} \exp\left[\left(\frac{E_x}{R}\right)\left(\frac{1}{T_b} - \frac{1}{T_{0x}}\right)\right] \tag{5}$$

where η_{bx} and η_{0x} are the viscosities of each component at the binder temperature T_b and T_{0x}. R is the gas constant and E_x is the viscous flow activation energy of each component [21], as shown in Table 1. The influence of temperature on the viscosity of feedstock is mainly reflected in the viscosity of binder.

Table 1
Viscosity properties of components of the binder.

Components	T_{0x}/K	η_{0x}/Pa·s	E_x/J·mol^{-1}
PW	373	0.009	4400
HDPE	463	300	26,300
SA	383	0.007	0

The viscosity of the binder system can be calculated by the superposition principle [22,23]:

$$\ln(\eta_b) = \sum_{i=1}^{n} W_i \ln(\eta_{bi}) \tag{6}$$

where W_i is the weight fraction of each component.

Study by Manninen [24] showed that the viscosity of binder and powder agreed with the additive principle:

$$\eta_f = \phi_b \eta_b + \phi_p \eta_p \tag{7}$$

where η_p is the powder viscosity. According to Eqs. (4)–(7), the powder viscosity can be obtained.

2.3. Powder–binder drag force

In the two-phase model, the drag force [25,26] between binder and powder is defined as:

$$\mathbf{F_{bp}} = \frac{1}{2} C_D A_p \rho_{bp} \left|\boldsymbol{v_p} - \boldsymbol{v_b}\right| \left(\boldsymbol{v_p} - \boldsymbol{v_b}\right) \tag{8}$$

where C_D is the drag coefficient, A_p is the area of a single particle projected in the flow direction, $A_p = \dfrac{\pi d_p^2}{4}$, d_p is the particle mean diameter, ρ_{bp} is the mixture density, and $\rho_{bp} = \phi_b \rho_b + \phi_p \rho_p$.

The drag coefficient [25,26] is defined as:

$$C_D = \frac{24}{Re_p}\left(1 + 0.15 Re_p^{0.687}\right) + \frac{0.42}{1 + 42500 Re_p^{-1.16}} \quad \text{for } Re_p < 2 \times 10^5. \tag{9}$$

The magnitude of drag force is primarily dictated by the particle Reynolds number [26], defined as:

$$Re_p = \frac{\rho_{pb} d_p \left|\mathbf{w_{pb}}\right|}{\eta_f} \tag{10}$$

where $\mathbf{w_{pb}}$ is the relative velocity between powder and binder, and $|\mathbf{w_{pb}}| = |\boldsymbol{v_p} - \boldsymbol{v_b}|$.

When the viscosity of feedstock is influenced by the feedstock temperature and the shear strain rate, Re_p changes, resulting in the change of drag force between powder and binder. Furthermore, the different velocities of binder and powder will be obtained with numerical calculation of the continuity equations, leading to the powder–binder separation.

2.4. Energy exchange between the phases

In the two-phase model, energy exchange between the phases is made mainly of interphase heat transfer. The rate of interphase heat transfer between binder and powder Q_{bp} is defined as:

$$Q_{bp} = h_{bp} A_p \left|T_p - T_b\right| \tag{11}$$

where T_p is the temperature of phase powder, and h_{bp} is an overall heat transfer coefficient, defined as:

$$h_{bp} = \frac{\left(\phi_b \lambda_b + \phi_p \lambda_p\right) N_u}{d_p} \tag{12}$$

where N_u is the Nusselt number, $N_u \approx 2$. λ_b and λ_p are the heat transfer coefficient of phase binder and powder, respectively. The thermo-physical properties of powder phase and binder phase are listed in Table 2.

3. Experimental procedures

The powder used in this study was 316L SS (Handan ASL Atomized Powder Co., China), with a particle average diameter of 8.0 μm, and pycnometric density of 7930 kg·m^{-3}. Fig. 1 shows SEM micrograph of 316L SS powder. The selected binder system was composed of 69% (weight fraction) paraffin wax (PW), 30% polypropylene (HDPE) and 1% stearic acid (SA). The densities of PW, HDPE and SA are 910 kg·m^{-3}, 980 kg·m^{-3}, and 960 kg·m^{-3}, respectively.

The feedstock was prepared in the XSM1/20–80 rubber mixer at a rotational speed of 100 r·min^{-1} at 433 K for 120 min, with 61% powder loading. After mixing, viscosity of prepared feedstock was measured in the RH2000 capillary rheometer within a range of shear rate from 20 to 10,000 s^{-1} at 423 K, 443 K and 463 K, respectively. As shown in Fig. 2, the viscosity versus the shear strain rate was a log–log relationship. Furthermore, the factors n and $K_{\phi D}$ of the viscosity model were obtained through the curve fitting method, n = 0.352, and $K_{\phi D} = 5.32 \times 10^4$. There was a good agreement between the experimental data and model calculated results, which assured obtaining of reliable results of the numerical simulation.

Green bodies were prepared in the horizontal CJ80E molding machine in the temperature range from 423 K to 473 K, the injection rate range from 20 to 90 cm^3·s^{-1}, the mold temperature 333 K. The samples were bricks with dimensions of $28 \times 20 \times 6$ mm, as shown in Fig. 3(a). In this study, green bodies were scanned by the combination set up of the 130 keV micro-focus X-Ray tube and image intensifier/charged coupled device (CCD) camera detector, with the tube energy of 120 keV and current of 0.235 mA. X-Ray reconstructed slice image of middle cross section in the green body was shown in Fig. 3(c). Gray values of reconstructed image can be used to evaluate quantitatively the density variations because of the variations in X-Ray absorption seen between different densities. A linear correlation between the actual density and the green value exists, and Yang [10] proposed a method to obtain the actual density distribution of tested green body. The same method was used in this study.

In X-Ray tomographic reconstructed images, noise does always exist. In order to handle impulse noise, the mean gray value of rectangular window was used to characterize the local density, as shown in Fig. 3(c). In this study, the rectangular window size was 5×5 pixels. The density of feedstock was relative to the powder volume fraction in the corresponding area. Fig. 4 showed the relationship between the powder volume fraction and the gray value along line L in the X-Ray CT reconstructed image.

4. Numerical simulation

Based on the model of mold filling in the second section, ANSYS-CFX 13 software was used to simulation the mold filling in PIM. The geometry shape and mesh of mold were shown in Fig. 3(b). Tetrahedral mesh was generated with 50,615 elements and 19,657 nodes. The middle section for simulation analysis and the size of gate cross section were

Table 2
Thermo-physical properties of the powder and binder components.

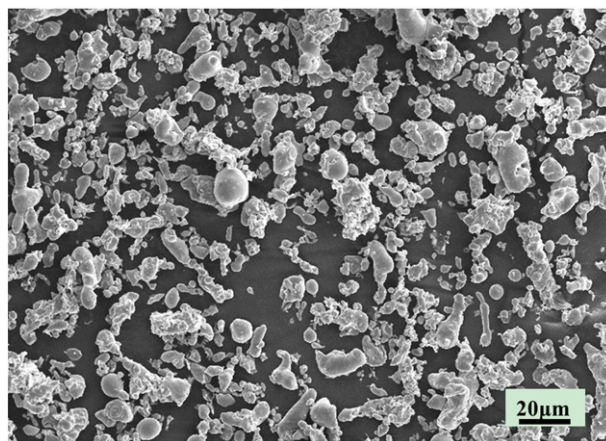| Components	Thermal conductivity/W·m^{-1}·K^{-1}	Specific heat capacity/J·K^{-1}·kg^{-1}
PW	0.14	2700
HDPE	0.30	2200
SA	0.35	1700
316 L SS	16.2	500

Fig. 1. SEM micrograph of 316L SS powders.

shown in Fig. 3(d). Model parameters and simulation process parameters were listed in Table 3. The initial conditions and boundary conditions were based on the experimental conditions. In this work, Mass Flow Inlet boundary condition was used in CFX 13. And injection rate 20–90 cm^3·s^{-1} corresponded to mass flow rate 0.103–0.464 kg·s^{-1}. At the inlet boundary, mass flow rate, initial powder contents ϕ_{p0} and initial binder contents ϕ_{b0} were assigned. At the outlet boundary, atmosphere pressure was imposed. At the wall boundary, the assigned wall temperature represented the mold temperature. In the mold, the initial powder and binder contents were zero. The total simulation time was 0.15 s, and the time step was 0.0015 s.

5. Results and discussion

According to the mold filling model, it can be believed that the powder–binder separation was related to feedstock temperature, shear rate, drag coefficient, etc. Line L in the middle section was selected to investigate distributions of the related parameters. In this study, the results of experiments and simulations were compared in the same region, as shown in Fig. 3.

5.1. Effects of temperature on the powder–binder separation

The viscosity of feedstock is very sensitive to temperature. In this study, green bodies were prepared in a wide temperature range, from 423 K to 473 K. To investigate the effects of temperature, the same injection rate 60 cm^3·s^{-1} was selected. As shown in Fig. 5(a), in the middle part of Line L, the temperature of each case was nearly the same as the initial feedstock temperature, and in the two sides of L, a temperature gradient existed. Obviously, the temperature gradient would decrease
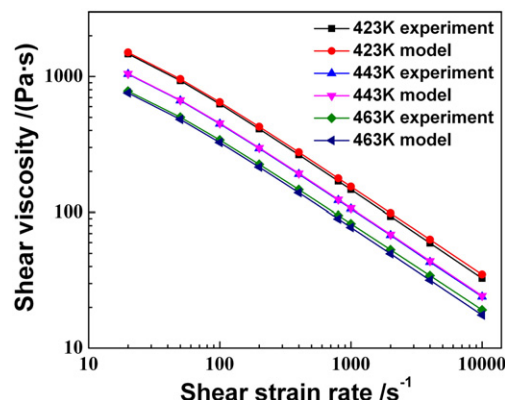

Fig. 2. Shear viscosity of the feedstock by the experiments and the model calculations.
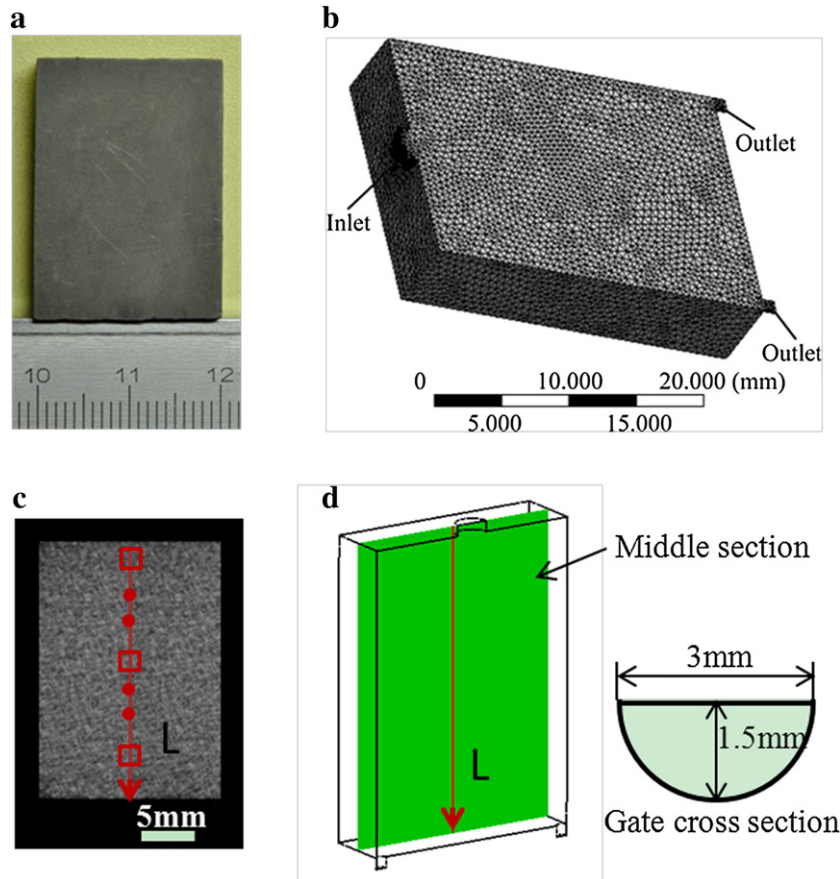
Fig. 3. (a) Green body. (b) Geometry shape and mesh of mold. (c) X-Ray reconstructed slice image of middle section in the green body. (d) Middle section for simulation analysis and size of gate cross section.

as the mold temperature increased, which was beneficial to rheological property but meant longer cooling time. In Fig. 5(b), the shear strain rate of each case had the similar trend, and reached the peak value about 3600 s^{-1} at a distance of about 0.0025 m. The occurrence of this phenomenon was due to the relative position of gate and middle section, as shown in Fig. 3(d). The shear strain rate was high in the early arrival area of feedstock. When the distance was greater than 0.0025 m, the shear strain rate of high temperature case was higher than that of low temperature case. When the temperature was 473 K, the shear strain rate was the maximal. Under the combined action of temperature and shear strain rate, there were very low viscosities from 18 Pa·s to 130 Pa·s in the middle of L in the 473 K case, as shown in Fig. 5(c). According to Eqs. (9) and (10), the lower viscosity meant the lower drag

coefficient, as shown in Fig. 5(d). The magnitude of drag force between powder and binder was primarily influenced by the drag coefficient [26]. Low drag force resulted in a high relative velocity between powder and binder, as shown in Fig. 5(f), which was the reason for the powder–binder separation. Although the initial injection rates of six temperature cases were the same, the powder velocities were different, owing to the different interactions between powder and binder in different cases. The powder volume fractions (PVFs) of experimental and numerical results were shown in Fig. 5(g) and (h), respectively. At the beginning of L, near the gate, there were binder accumulation regions in all cases. At the end of L, near the mold wall, the PVFs were complex in six cases, $PVF_{443K} > PVF_{453K} > PVF_{433K} > PVF_{423K} > PVF_{463K} > PVF_{473K}$. Besides, the PVFs of 463 K case and 473 K case were lower than 0.61, the powder loading. Although the experimental results had a more evident boundary layer effect, and were more fluctuant, the similar phenomena were found in the experimental data.

In order to understand the above-mentioned results, evolution of the powder content in the middle section was investigated, as shown in Fig. 6. The range of PVF was selected from 0.6 to 0.612, so as to
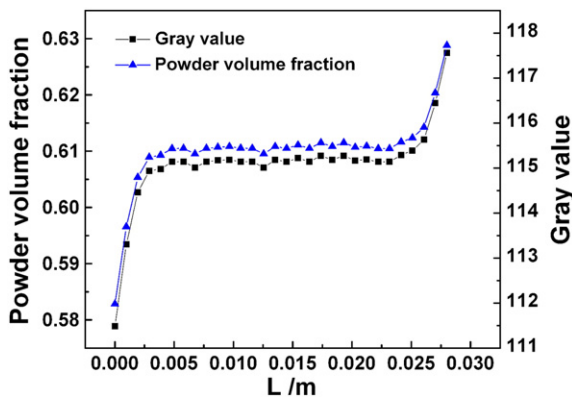

Fig. 4. The relationship between the powder volume fraction and the gray value along line L in the CT reconstructed image.

Table 3
Model parameters and simulation process parameters.

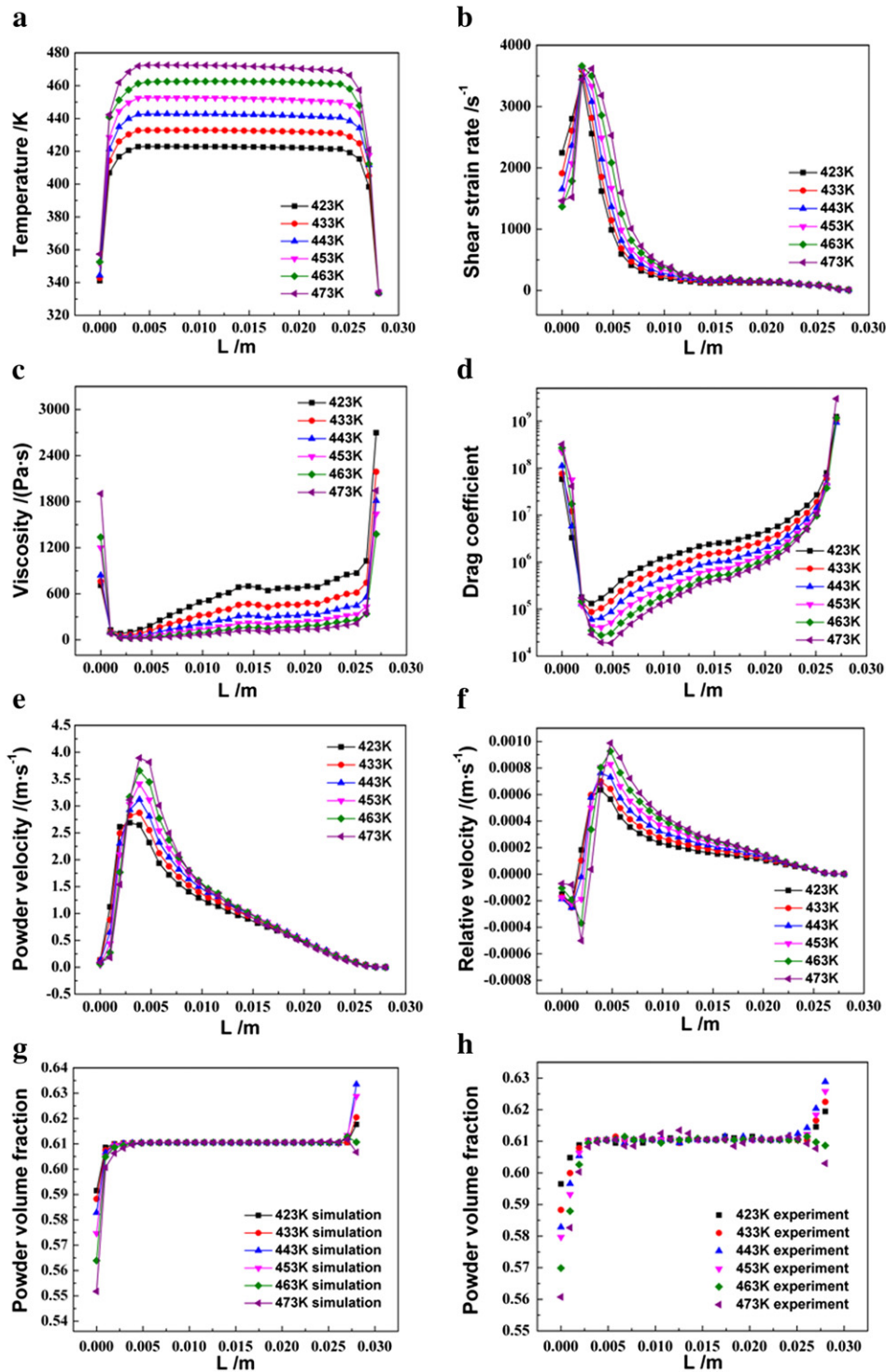|	
R	8.314 J·mol^{-1}·K^{-1}
n	0.352
$K_{\phi D}$	5.36×10^4
ϕ_{b0}	0.39
ϕ_{p0}	0.61
d_p	8.0×10^{-6} m
Temperature range	423–473 K
Injection rate range	20–90 cm^3·s^{-1}
Mold temperature	333 K

Fig. 5. Parameter distributions along line L in the middle section at the injection rate 60 cm³·s⁻¹. (a) Temperature. (b) Shear strain rate. (c) Viscosity. (d) Drag coefficient. (e) Powder velocity. (f) Relative velocity between powder and binder. (g) Powder volume fraction of numerical results. (f) Powder volume fraction of experimental results.

observe the powder–binder separation obviously. There were incompact regions around the compact regions. And the incompact regions would be compacted in the subsequent stage. In the initial stage of molding filling, the shear strain rate was high near the gate region, resulting in a very low viscosity of feedstock. The powder obtained a faster speed than the binder and had a rich content in the flow front, as the drag force between binder and powder decreased. Powder contents were higher than 0.61 in the flow front, which could be observed in the time 0.0075 s at each temperature case. In the temperature 423 K case, the flow front, with powder content higher than 0.60,

moved about 9 mm and stopped moving forward. Then, the filling feedstock accumulated until nearly reached the gate region. Later, the feedstock was pushed to two sides closed to the wall. Meanwhile, an interesting phenomenon was observed, the powder–binder separation weakened as feedstock with the rich binder content was pushed from two sides to the front. In the end, the feedstock packed the mold. In the 443 K case, a similar process occurred, and it was observed that the width of compacting feedstock maintained until the next stage, as shown in Fig. 6 443 K–0.015 s. The minimum viscosities of 423 K, 443 K, 473 K cases were 82 Pa·s, 46 Pa·s and 18 Pa·s, respectively. In
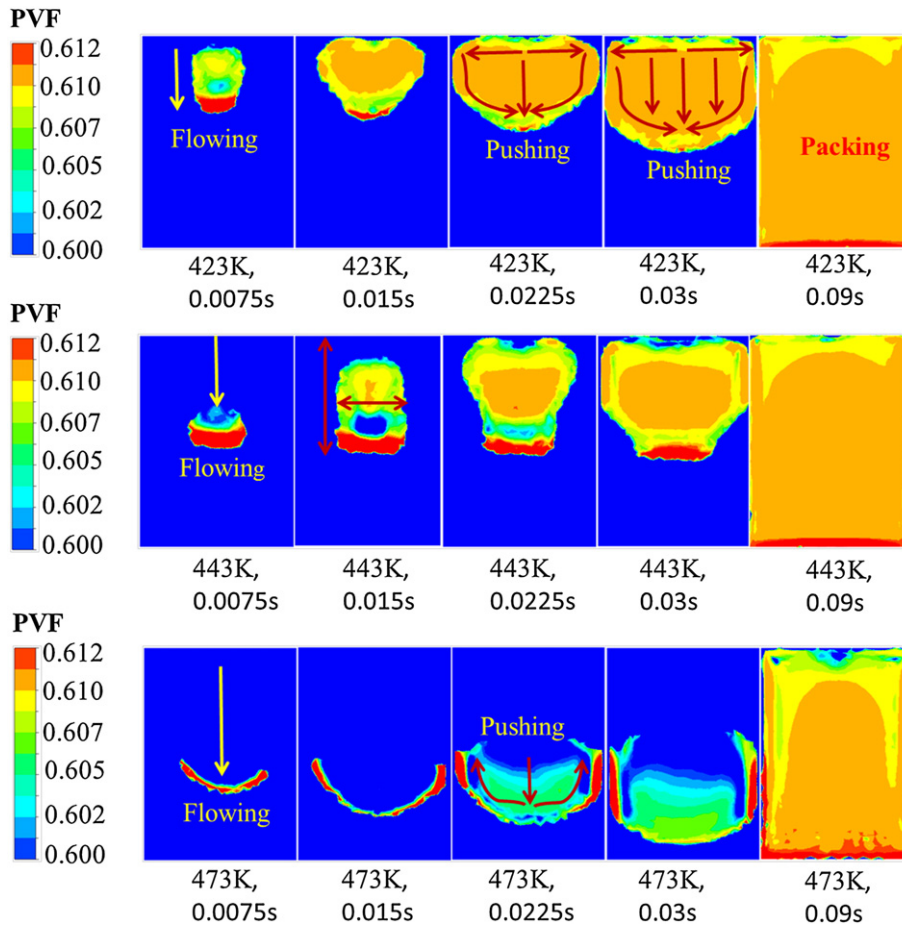
Fig. 6. Evolution of the powder content in the middle section of 423 K, 443 K and 473 K cases, at the injection rate 60 cm³·s⁻¹.

the temperature 473 K case, the particles in the flow front were pushed to both sides, and accumulated at both sides, as shown in Fig. 6. A small part of binder accumulated in the bottom, which was different from other cases. Meanwhile, powder–binder separation was more serious than other cases, and the same phenomenon was detected by X-Ray CT as shown in Fig. 5(h). When the temperature increased, the viscosity of feedstock decreased, resulting in the more serious powder–binder separation and a longer stop distance, and the powder content near the bottom increased along with the increased temperature. When the temperature was higher than 453 K, the viscosity of feedstock was lower than 40 Pa·s. As a result, the particles were pushed to both sides, and the powder content near the bottom decreased along with the increased temperature. The experimental phenomena were explained clearly by the evolution of powder–binder separation obtained with numerical simulation method. In this study, the compacted regions were selected to investigate, and the filling pattern of PIM was summarized as: Flowing–Pushing–Packing–Cooling.

5.2. Effects of injection rate on the powder–binder separation

In this study, the effects of injection rates on the powder–binder separation were investigated. Selected green bodies were prepared at the temperature 433 K and the injection rate 30 cm³·s⁻¹, 45 cm³·s⁻¹, 60 cm³·s⁻¹, 75 cm³·s⁻¹ and 90 cm³·s⁻¹, respectively. The numerical calculation and experiment results were shown in Fig. 7. Temperatures in each case were similar due to the same initial feedstock temperature. In the 30 cm³·s⁻¹ case, longer time was required to fill mold because of

the lower injection rate, so a slight temperature drop was observed due to the cooling effect. The maximal shear strain rates varied with injection rates were 1718 s⁻¹, 2522 s⁻¹, 3540 s⁻¹, 4321 s⁻¹ and 5202 s⁻¹, respectively, as shown in Fig. 7(b). The shear strain rate increased in proportion to the injection rate. In the 30 cm³·s⁻¹ case, viscosities were obviously higher than other cases, because of the nonlinear relationship between the viscosity and the shear rate, according to Eq. (4). The minimal viscosities varied with the injection rates were 94 Pa·s, 69 Pa·s, 59 Pa·s, 54 Pa·s and 48 Pa·s, respectively, as shown in Fig. 7(c). Similar to the analysis of Section 5.1, when the viscosities were lower, the powder–binder separation phenomena were more likely to occur. In the 90 cm³·s⁻¹ case, the powder velocity and absolute value of powder–binder relative velocity were greater than others, leading to more serious inhomogeneity. As shown in Fig. 7(g), the higher the injection rate was, the more serious the powder–binder separation was. Although the experimental data was more fluctuant, the similar trend was found, as shown in Fig. 7(h).

Evolution of powder content in the middle section at different injection rates were investigated, as shown in Fig. 8. Owing to the different injection rates, corresponding time was selected to insure the same amount of filling feedstock. In the 30 cm³·s⁻¹ case, powder content is lower than binder content in the flow front, and the initial compacted region was near the gate. In the 60 cm³·s⁻¹ and 90 cm³·s⁻¹ case, the initial compacted region was in the middle of mold. When the injection rate was higher, the flow front of feedstock had the higher powder content, longer stop-moving distance from the gate and greater width. Compared to the temperature, the injection rate had smaller effect on
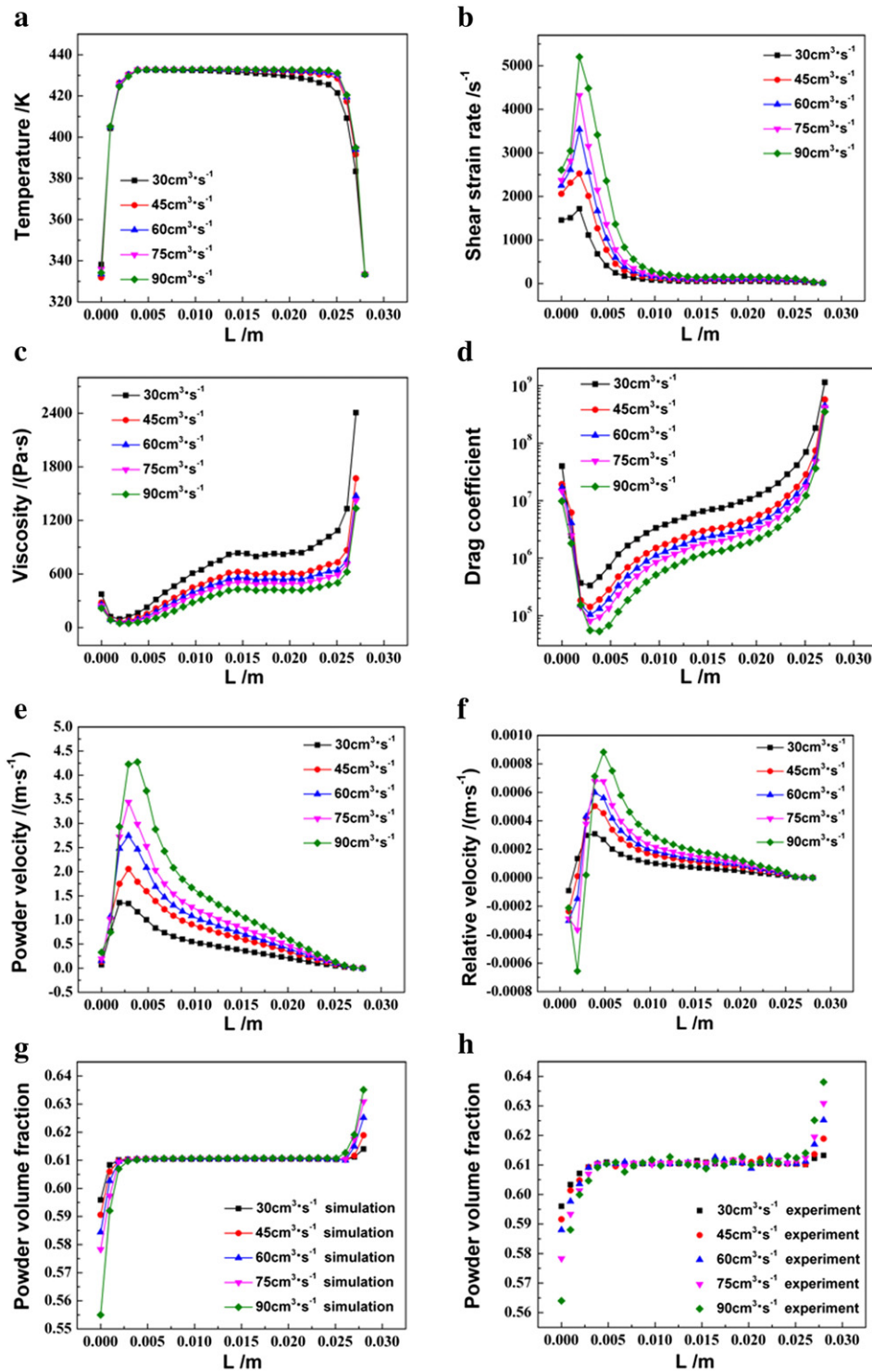
Fig. 7. Parameter distributions along line L in the middle section at the temperature 433 K. (a) Temperature. (b) Shear strain rate. (c) Viscosity. (d) Drag coefficient. (e) Powder velocity. (f) Relative velocity between powder and binder. (g) Powder volume fraction of numerical results. (f) Powder volume fraction of experimental results.

filling patterns due to smaller effect on viscosity in this study, in the temperature range from 423 K to 473 K, and injection rate range from 30 cm³·s⁻¹ to 90 cm³·s⁻¹.

5.3. Compacting filling patterns of PIM

Obviously, there were incompact regions around the compact regions. The incompact regions would be compacted in the subsequent stage. Therefore, the compacted regions were selected to investigate

the compacting filling patterns in powder injection molding. In this study, the regions where powder contents reached 0.6 were considered as compacted regions. According to the analysis of filling mold in Sections 5.1 and 5.2, a typical compacting filling pattern of powder injection molding was proposed, as shown in Fig. 9. In the initial stage of filling mold, the feedstock got a high speed and flowed in the mold. Powders maintained a faster speed than binder and accumulated in the flow front. Owing to the drag forces, the flow front moved a certain distance and stopped moving forward. Then, the filling feedstock
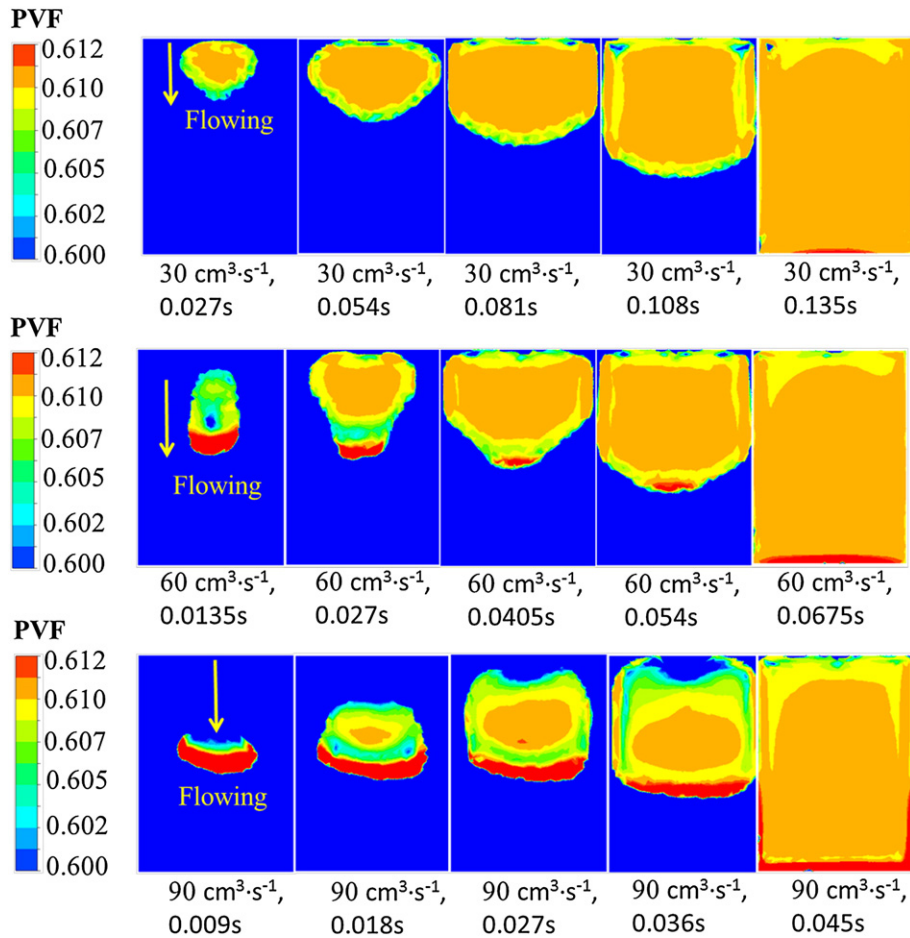
Fig. 8. Evolution of the powder content in the middle section at the injection rate 30 cm³·s⁻¹, 60 cm³·s⁻¹ and 90 cm³·s⁻¹ cases, the same temperature 433 K.

accumulated until nearly reached the gate region, as shown in Fig. 9(b). Meanwhile, the length L_1 and width L_2 maintained nearly the same until the next stage. The length L_1 and width L_2 depended on the viscosities and velocities of feedstock. The phenomenon was obviously exhibited in Fig. 6. Later, the feedstock was pushed to two sides closed to the wall, and moved forward. The powder–binder separation weakened as feedstock with the rich binder content was pushed from two sides to the front. In the end, the feedstock packed the mold. The compacting filling pattern is particular to powder injection molding, compared with plastic injection molding. It is helpful to understand the evolution of powder–binder separation.

The initial impacting area ratio in the middle section was defined as:

$$S_C = \frac{L_1 L_2}{LW} \tag{13}$$

where L and W were the length and width of the middle section, L_1 was the distance from the motionless compacted front to the top wall and L_2 was the width of compacted feedstock. In order to reduce the effect of interaction between the feedstock and wall, high temperatures at the low injection rates and low temperatures at the high injection rates were selected to ensure a small S_C value, for the purpose of high
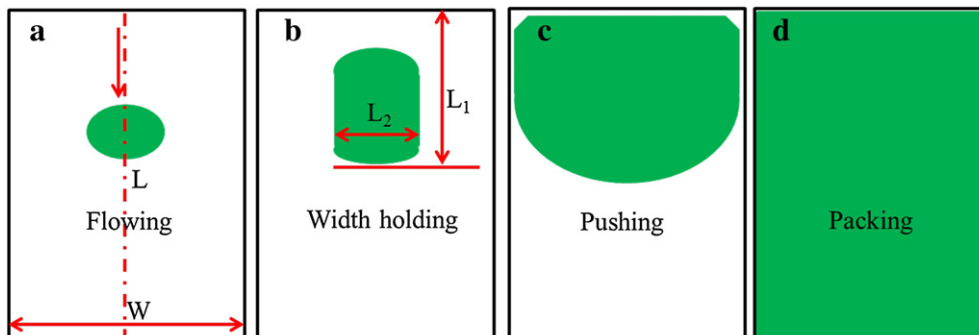

Fig. 9. A typical compacting filling pattern of powder injection molding.
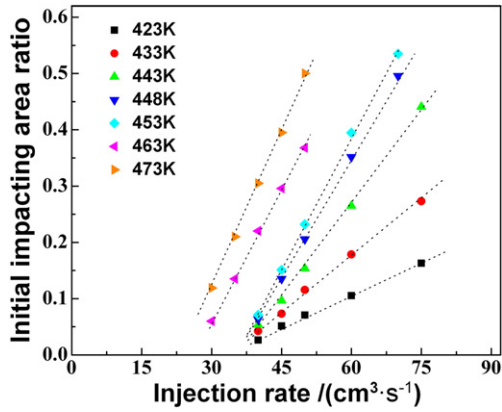
Fig. 10. The initial impacting area ratio in the middle section at each process condition.

accuracy. The length of L_1 and L_2 was measured at each process condition, and the values of S_C were calculated, as shown in Fig. 10. It was a linear function between S_C and injection rate at each temperature. The function was expressed as:

$$S_{CT} = b_0 + k_T v_{IR} \qquad (14)$$

where S_{CT} was the value of S_C at the temperature T, v_{IR} was the injection rate of feedstock, slope k_T was the change rate of S_{CT} versus v_{IR} and b_0 was a constant. At low temperatures, such as 423 K, S_{CT} increased slowly with the rising injection rate, that is to say, k_T was small at the low temperatures. Typically, it was observed that the higher temperature resulted in the greater k_T value. Furthermore, it was observed that k_T increased slowly when the temperature was higher than 448 K. When the temperature and injection rate were selected, it was easy to predict the initial impacting area ratio in Fig. 10. In general, when $S_{CT} < 0.1$, the initial compact region was near the gate; when $0.1 < S_{CT} < 0.6$, the initial compact region was in the middle of cavity; when $S_{CT} > 0.6$, the initial compact region was likely to near the bottom or two sides of cavity. Of course, the initial compact region also depended on the geometry shape of cavity. The value of S_{CT} was helpful to predict the compacting filling patterns, furthermore, to understand the powder–binder separation in powder injection molding. According to the results and discussion in this work, the bigger value of S_{CT} meant the more serious powder–binder separation.

For a certain feedstock, filling patterns of powder injection molding mainly depended on the temperature, injection rate, and features of gate and mold cavity. A filling mobility variable of feedstock was proposed as follows:

$$V_{FM} = \frac{v_{IR}}{\eta_{CT} S_{GCS}} \qquad (15)$$

where η_{CT} was defined as the feedstock viscosity at temperature T and shear strain rate 1000 s^{-1}, S_{GCS} was the cross section area of the gate, v_{IR}/S_{GCS} was the velocity of feedstock in the gate indeed. Hence, the filling mobility variable of feedstock was mainly relative to the viscosity and velocity of the feedstock. The value of V_{FM} was

proportional to the velocity of feedstock and inversely proportional to the viscosity of feedstock. The unit of V_{FM} was m$^2 \cdot$ kg^{-1}.

At a certain temperature, η_{CT} of feedstock was fixed. The Eq. (14) can be expressed as:

$$S_{CT} = b_0 + (k_T \eta_{CT} S_{GCS}) \frac{v_{IR}}{\eta_{CT} S_{GCS}}. \qquad (16)$$

The initial impacting area ratio factor of the middle section was defined as:

$$f_{IIART} = k_T \eta_{CT} S_{GCS}. \qquad (17)$$

The Eq. (16) can be expressed as:

$$S_{CT} = b_0 + f_{IIART} V_{FM}. \qquad (18)$$

The factor f_{IIART} was the rate of change of S_C versus V_{FM}. The value of f_{IIART} was proportional to the k_T and η_{CT}, which was relative to the filling mobility of feedstock and homogeneity of prepared part at temperature T. The unit of f_{IIART} is kg$\cdot$m^{-2}. When the section was given a thickness $\triangle$m, it was easier to understand the meaning of f_{IIART}.

The values of f_{IIART} were calculated at each temperature, as shown in Table 4. In this study, the values of f_{IIART} increased with the rising of temperature, and reached the peak between 443 K and 453 K, then, decreased with the rising of temperature. The factor f_{IIART} gave a comprehensive evaluation of feedstock filling mobility and homogeneity at temperature T. The temperature at which f_{IIART} reached the peak could be used as the proper injection temperature. In this study, the results showed that the temperature range 443–453 K was the proper injection temperature range, which was consistent to practical experience.

6. Conclusion

Through the above analysis, the following results were summarized:

➢ The mold filling model of PIM has been developed, based on the multiphase fluid theory and the feedstock viscosity model. Variations of the feedstock viscosity and the powder–binder drag force lead to the powder–binder separation. The evolution of phase separation was obtained by numerical simulation of injection molding, which was helpful to explain the experimental phenomena.
➢ The filling mobility variable was proportional to the velocity of feedstock and inversely proportional to the viscosity of feedstock. The initial impacting area ratio factor represented feedstock mobility and homogeneity at a certain temperature. Based on these proposals, a preliminary compacting filling pattern theory of powder injection molding was developed.
➢ For a certain feedstock, the temperature at which f_{IIART} reached the peak could be used as the proper injection temperature.

Table 4
The initial impacting area ratio factor at each temperature.

Temperature/K	423	433	443	448	453	463	473
f_{IIART}/(kg$\cdot$m^{-2})	2.27	3.05	3.55	3.9	3.78	2.87	2.07

References

[1] Z.Y. Liu, N.H. Loh, S.B. Tor, K.A. Khor, Characterization of powder injection molding feedstock, Mater. Charact. 49 (2002) 313–320.

[2] S. Ahn, S.J. Park, S. Lee, S.V. Atre, R.M. German, Effect of powders and binders on material properties and molding parameters in iron and stainless steel powder injection molding process, Powder Technol. 193 (2009) 162–169.

[3] Q. Wang, H. Yin, X. Qu, J.L. Johnson, Effects of mold dimensions on rheological of feedstock in micro powder injection molding, Powder Technol. 193 (2009) 15–19.

[4] M.E. Sotomayor, A. Várez, B. Levenfeld, Influence of powder particle size distribution on rheological properties of 316 L powder injection moulding feedstocks, Powder Technol. 200 (2010) 30–36.

[5] Y. Li, L. Li, K.A. Khalil, Effect of powder loading on metal injection molding stainless steels, J. Mater. Process. Technol. 183 (2007) 432–439.

[6] C. Quinard, J. Song, T. Barriere, J.C. Gelin, Elaboration of PIM feedstocks with 316 L fine stainless steel powders for the processing of micro-components, Powder Technol. 208 (2011) 383–389.

[7] R. Supati, N. Loh, K. Khor, S. Tor, Mixing and characterization of feedstock for powder injection molding, Mater. Lett. 46 (2000) 109–114.

[8] P. Suri, S.V. Atre, R.M. German, J.P. de Souza, Effect of mixing on the rheology and particle characteristics of tungsten-based powder injection molding feedstock, Mater. Sci. Eng. A 356 (2003) 337–344.

[9] O. Weber, A. Rack, C. Redenbach, M. Schulz, O. Wirjadi, Micropowder injection molding: investigation of powder–binder separation using synchrotron-based microtomography and 3D image analysis, J. Mater. Sci. 46 (2011) 3568–3573.

[10] S. Yang, R. Zhang, X. Qu, X-ray tomographic analysis of powder–binder separation in SiC green body, J. Eur. Ceram. Soc. 33 (2013) 2935–2941.

[11] A. Mannschatz, S. Hohn, T. Moritz, Powder–binder separation in injection moulded green parts, J. Eur. Ceram. Soc. 30 (2010) 2827–2832.

[12] Ç. Karataş, A. Sözen, E. Arcaklioglu, S. Erguney, Investigation of mouldability for feedstocks used powder injection moulding, Mater. Des. 29 (2008) 1713–1724.

[13] T.S. Shivashankar, R.K. Enneti, S.-J. Park, R.M. German, S.V. Atre, The effects of material attributes on powder–binder separation phenomena in powder injection molding, Powder Technol. 243 (2013) 79–84.

[14] T. Barrière, J.-C. Gelin, B. Liu, Improving mould design and injection parameters in metal injection moulding by accurate 3D finite element simulation, J. Mater. Process. Technol. 125 (2002) 518–524.

[15] S. Kim, S.J. Park, S.V. Atre, R.M. German, Simulation of binder–powder separation in powder injection molding, 2007 International Conference on Powder Metallurgy and Particulate Materials, PowderMet 2007, May 13, 2007–May 16, 2007, Metal Powder Industries Federation, Denver, CO, United states, 2007, pp. 18–114.

[16] A. Greiner, D. Kauzlarić, J.G. Korvink, R. Heldele, M. Schulz, V. Piotter, T. Hanemann, O. Weber, J. Haußelt, Simulation of micro powder injection moulding: powder segregation and yield stress effects during form filling, J. Eur. Ceram. Soc. 31 (2011) 2525–2534.

[17] S.K. Samanta, H. Chattopadhyay, M.M. Godkhindi, Modelling the powder–binder separation in injection stage of PIM, Prog. Comput. Fluid Dyn. 11 (2011) 292–304.

[18] V.V. Bilovol, L. Kowalski, J. Duszczyk, L. Katgerman, The effect of constitutive description of PIM feedstock viscosity in numerical analysis of the powder injection moulding process, J. Mater. Process. Technol. 178 (2006) 194–199.

[19] C. Binet, D.F. Heaney, R. Spina, L. Tricarico, Experimental and numerical analysis of metal injection molded products, J. Mater. Process. Technol. 164–165 (2005) 1160–1166.

[20] J. Koszkul, J. Nabialek, Viscosity models in simulation of the filling stage of the injection molding process, J. Mater. Process. Technol. 157–158 (2004) 183–187.

[21] R.M. German, Powder Injection Molding, Metal Powder Industries Federation, Princeton, 1990.

[22] J. Shah, R.E. Nunn, Rheology of metal injection molding feedstock, Powder Metall. Int. 19 (1987) 38–40.

[23] S.L. Li, Y.M. Li, X.H. Qu, B.Y. Huang, Rheological properties of metal injection molding feedstock, Trans. Nonferrous Metals Soc. China 12 (2002) 105–108.

[24] M. Manninen, V. Taivassalo, S. Kallio, On the Mixture Models for Multiphase Flow, VTT Publications, Espoo, 1996.

[25] A. Haider, O. Levenspiel, Drag coefficient and terminal velocity of spherical and nonspherical particles, Powder Technol. 58 (1989) 63–70.

[26] E. Loth, Drag of non-spherical solid particles of regular and irregular shape, Powder Technol. 182 (2008) 342–353.